ADVANCED FUNCTIONAL MATERIALS
www.afm-journal.de

Near-Infrared Light-Programmable Negative Differential Transconductance in Organic Electrochemical Transistors for Reconfigurable Logic

Debdatta Panigrahi, Christina J. Kousseff, Aristea Pavlou, Zeinab Hamid, Iain McCulloch, Fabrizio Toricelli, Paul W. M. Blom, and Paschalis Gkoupidenis**

Organic electrochemical transistors offer advantages in low-power, ion-mediated electronics, yet their typically monotonic transfer characteristics limit their integration into advanced information-processing systems. Here, the emergence of optically induced negative differential transconductance (NDT) is reported in organic electrochemical transistors based on a near-infrared responsive polymer, p(C_4DPP-T), and a potassium iodide electrolyte. Under near-infrared illumination, the device exhibits a transition from a conventional monotonic transfer characteristic to a non-monotonic one with three conductance regions: a conventional binary on/off, a ternary on/partially on/off state, and an on/on/off, depending on light intensity. This unique response stems from the intrinsic material properties of the system, where near-infrared illumination generates holes in p(C_4DPP-T) and the potassium iodide electrolyte drives redox reactions. These coupled processes modulate channel doping, inducing NDT. Notably, NDT behavior is achieved without complex device architectures or p–n heterojunctions, which are typically required in conventional field-effect transistors. It is further shown that enlarging the gate–electrolyte interfacial area enhances the NDT response, yielding higher peak currents, sharper transitions, and improved peak-to-valley ratios. Finally, an optically reconfigurable logic circuit capable of switching between binary and ternary logic is realized without altering the device architecture, paving the way for the development of adaptive electronic circuits.

1. Introduction

Organic electrochemical transistors (OECTs) have garnered significant attention in recent years as key components in bioelectronics, iontronic sensors, neuromorphic devices, and low-power logic circuits.[1–6] Their ability to modulate channel conductance through ionic interactions with an electrolyte distinguishes them from conventional field-effect transistors, enabling high transconductance at low operating voltages and compatibility with aqueous environments. These characteristics make OECTs uniquely suited for interfacing with biological systems and for performing analog computations where energy efficiency is critical.[7,8] However, most OECTs exhibit a monotonic dependence of drain current (I_D) on gate voltage (V_G), typically showing either accumulation or depletion-mode behavior depending on the semiconductor and ion transport dynamics. While this monotonic response suffices for basic switching or sensing tasks, it constrains the broader adoption of OECTs in more advanced information processing

D. Panigrahi, A. Pavlou, P. W. M. Blom, P. Gkoupidenis
Department of Molecular Electronics
Max Planck Institute for Polymer Research
Ackermannweg 10, 55128 Mainz, Germany
E-mail: panigrahid@mpip-mainz.mpg.de; pgkoupi@ncsu.edu

C. J. Kousseff, Z. Hamid, I. McCulloch
Department of Chemistry
University of Oxford
12 Mansfield Road, Oxford OX1 3TA, UK

F. Toricelli
Department of Information Engineering
University of Brescia
Via Branze 38, Brescia 25123, Italy

I. McCulloch
Department of Electrical and Computer Engineering
Princeton University
41 Olden Street, Princeton, NJ 08544-0001, USA

P. Gkoupidenis
Department of Physics
North Carolina State University
2401 Stinson Dr, Raleigh, NC 27607, USA

The ORCID identification number(s) for the author(s) of this article can be found under https://doi.org/10.1002/adfm.202525271

DOI: 10.1002/adfm.202525271

systems that demand unconventional non-monotonic transfer characteristics.

Several emerging applications, including multivalued logic and spiking neuronal circuits, require devices capable of exhibiting multiple, discrete conductance states within a single transfer curve.[9–14] A non-monotonic current–voltage response, especially one featuring negative differential transconductance (NDT), allows I_D to increase, decrease, and rise again with increasing V_G, yielding three distinguishable output levels corresponding to "on", "partially on", and "off" states. These characteristics are critical for implementing a multivalued inverter circuit, compact multi-state memory, or emulating neuronal dynamics using minimal circuitry.[12–14] Although NDT behavior has been realized in a few solid-state devices via complex heterostructures, trap engineering, or tunneling-based mechanisms, these systems typically require high operating voltages and intricate fabrication processes, increasing device complexity and limiting energy efficiency.[15–20]

In comparison, achieving NDT in electrolyte-gated or OECT platforms remains limited and technically challenging. A few recent reports have shown three-state behavior with "Λ"-shaped transfer curves (off–on–off), yet such profiles are not suitable for full-swing logic-in-memory or multivalued logic applications.[21–28] Recently, Lim et al. demonstrated monolithically stacked vertical OECTs that exhibited electrochemically driven ternary conductance states through dual-channel coupling, further highlighting the potential of OECT platforms for multivalued logic, albeit at the cost of multilayer architectures and chemical modulation of PEDOT:PSS.[29] To overcome these constraints, a material- and environment-driven strategy is needed, one where the transfer characteristics of a simple, single-layer OECT can be dynamically modulated by an external stimulus, enabling multiple conductance states while preserving low-voltage operation.

In this work, we demonstrate the emergence of non-monotonic transfer characteristics in OECTs under optical excitation. By combining a near-infrared (NIR)-responsive semiconducting polymer, p(C_4DPP-T), with a potassium iodide (KI) electrolyte, we induce light-dependent changes in the transfer response of the device. In the absence of NIR illumination, the OECT displays typical p-type behavior with two well-defined states ("on" and "off"). Under low-intensity NIR light, the transfer curve evolves into a three-state response, where the I_D initially increases, then saturates, and finally increases again with increasing V_G. At higher illumination intensities, the device exhibits a pronounced NDT region at intermediate V_G. We attribute this behavior to light-induced hole generation in the polymer combined with the ability of iodine to form triiodide species, which together modulate interfacial redox dynamics and channel conduction. Notably, the device operates under a dual-mode gating: the conventional electrolyte gate modulates carrier density through ion injection, while the NIR light acts as an optical gate from the top, generating additional carriers via absorption in the active layer. This dual-input gating offers enhanced control over the device behavior. Light as a control stimulus is energy-efficient and allows precise spatiotemporal tuning, making it highly suitable for remote or parallel reconfiguration of logic states. Unlike electrical gating, it eliminates wiring constraints and enables localized activation, while also allowing global optical addressing to reconfigure multiple devices simultaneously. Moreover, beyond electrical operation, optical control provides a powerful contactless route to achieve such functionality.

Recent studies have demonstrated that light–matter interactions can effectively regulate the transconductance of OECTs, enabling photo-controlled amplification and gating behavior through photoactive or MOF-derived inorganic gates.[30–32] Moreover, 2D double van der Waals heterojunctions have exhibited optoelectronic NDT with ultrahigh peak-to-valley ratios and polarization-sensitive photoresponses, attributed to gate-modulated band-edge bending and photogating effects.[33–35] These reports collectively highlight the versatility of light-modulated charge transport in hybrid and multilayer systems, establishing the feasibility of optical control in transistor platforms. However, such devices rely on extrinsic photogating layers or precisely engineered heterointerfaces, whereas the present work achieves light-programmable NDT intrinsically within a single polymer channel via optically driven redox dynamics, without requiring any additional layers or hybrid interfaces. The use of NIR wavelengths further enhances the device's applicability, owing to their deep penetration and low scattering, which are advantageous for biomedical imaging, night-vision, and autonomous sensing applications.[36,37]

Beyond optical control, the magnitude and sharpness of the NDT response can be further tuned by varying the gate/electrolyte interfacial area. This establishes gate geometry as a structural design parameter for amplifying NDT characteristics. Finally, leveraging this optically tunable NDT behavior, we implement a light-reconfigurable logic circuit that transitions between binary and ternary logic states on demand, controlled solely by illumination intensity. Recent studies have demonstrated reconfigurable binary–ternary logic using dual-gate oxide transistors and photonic-modulated heterojunction devices, illustrating the potential of light as an external input for adaptive logic control.[38,39] Unlike these multilayer or hybrid systems, our approach realizes reconfigurability within a single polymer OECT, where optical excitation intrinsically modulates the redox-driven NDT through coupled ionic–electronic processes. This strategy provides an efficient route for light-controlled signal processing in organic electronics and opens new opportunities for adaptive, multifunctional, and neuromorphic circuits.

2. Results and Discussion

Figure 1 illustrates the design, material properties, and optoelectronic properties of the OECTs. Figure 1a shows the device configuration, where the source, drain, and gate electrodes are coplanar and patterned on the surface of a glass substrate. The semiconducting channel between the source and drain consists of a p-type conjugated polymer, p(C_4DPP-T), and an aqueous KI solution

P. Gkoupidenis
Department of Electrical and Computer Engineering
North Carolina State University
890 Oval Dr, Raleigh, NC 27606, USA
P. Gkoupidenis
Carbon Electronics Laboratories (ORaCEL)
North Carolina State University
Raleigh, NC 27695, USA

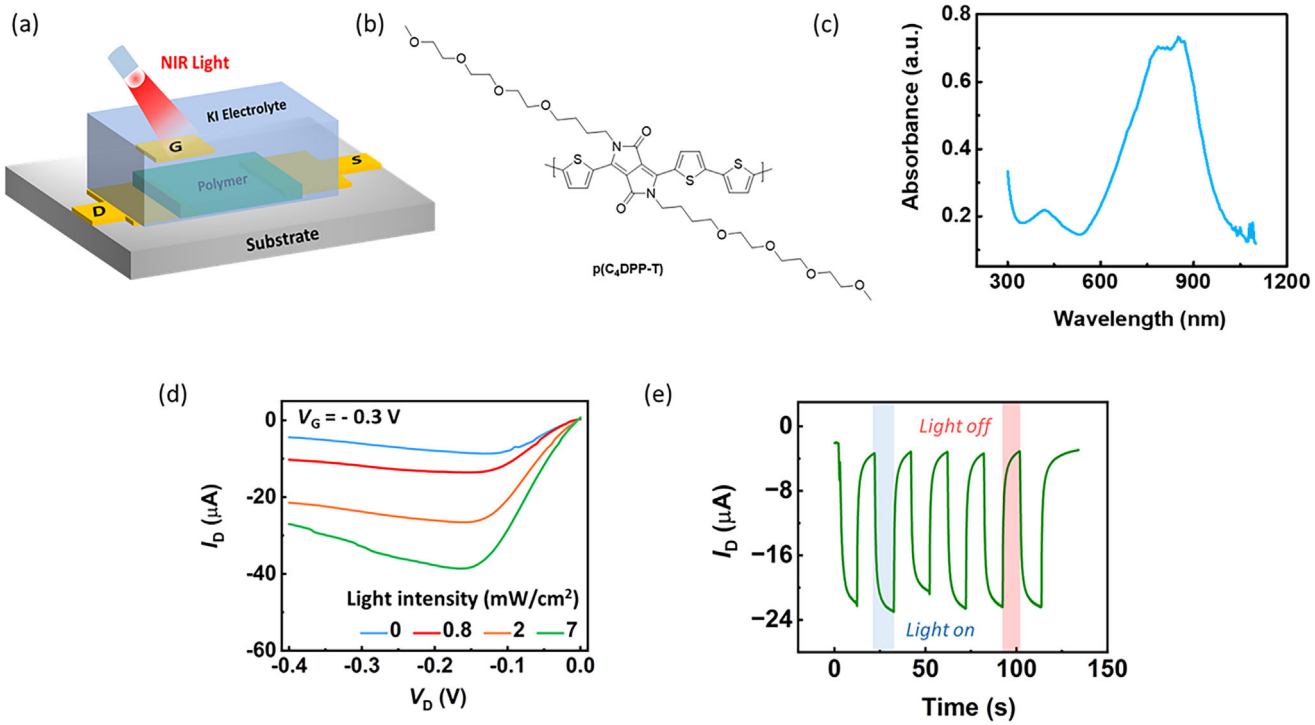

Figure 1. a) Schematic of the OECT device configuration. b) Chemical structure of the p(C_4DPP-T) polymer. c) Absorption spectrum of p(C_4DPP-T). d) Output characteristics of the OECT under dark and varying NIR illumination levels. e) Light-triggered switching behavior of the OECT under periodic NIR illumination.

serves as the electrolyte to facilitate ionic gating. NIR light is irradiated onto the polymer channel to explore light-triggered modulation of the device characteristics. Figure 1b shows the chemical structure of the p(C_4DPP-T) polymer, a newly synthesized material (synthetic details are provided in Note S1, Supporting Information). The surface morphology of the p(C_4DPP-T) film is shown in Figure S1 (Supporting Information).

The optical absorption spectrum of the polymer is shown in Figure 1c. The absorption spectrum exhibits a minor peak at 416 nm and strong absorption bands centered at 786 and 852 nm, confirming significant light harvesting in the NIR region. From the Tauc plot (Figure S2, Supporting Information), the optical band gap of p(C_4DPP-T) was quantitatively estimated to be ≈1.3 eV. Based on the optical characteristics, 850 nm NIR light was selected to excite the active semiconducting layer of the OECT. Figure 1d displays the output characteristics of the OECT both in the dark and under varying intensities of NIR illumination. A clear enhancement in I_D is observed with increasing light intensity, indicating that NIR light effectively modulates device behavior. At a fixed bias of $V_D = V_G = -0.3$ V, I_D increases significantly from −4 μA in the dark to −28 μA under 7 mW cm^{-2} illumination. This behavior highlights the role of light as an auxiliary gating mechanism, acting from the top of the device in addition to the electrochemical gating from the bottom. The results also indicate that NIR illumination leads to a higher hole density in the channel. Figure 1e shows the reversible switching behavior of the OECT under periodic NIR illumination at an intensity of 7 mW cm^{-2}. I_D initially remains ≈−3 μA in the dark, but rises to ≈−23 μA upon light exposure, attributed to photo-induced hole generation in the polymer. When the light is turned off, the current drops back to its initial value, suggesting gradual recombination of the photogenerated holes, restoring the original charge state of the channel. The rise and decay time constants were extracted as 1 s and 1.1 s, respectively (Figure S3, Supporting Information), highlighting the dynamic and reversible nature of the photoresponse. The obtained response time (≈1 s) is consistent with previously reported light-modulated OECTs, which generally exhibit photoresponse times ranging from a few hundred milliseconds to a few seconds depending on the device architecture and illumination conditions.[40–42] This confirms the light-tunable functionality of the device through optical illumination.

Figure 2 illustrates how NIR illumination transforms the transfer characteristics of OECTs, with panels 2(a–d) showing the evolution from conventional binary switching in the dark to a nonmonotonic three-state profile under increasing light intensity. Figure 2a shows the transfer characteristics in the absence of light, where the device exhibits typical p-type behavior functioning in the hole accumulation mode. I_D increases monotonically with the V_G, showing a clear "off" state with an I_D (= I_{OFF}) of ≈0.01 μA at the turn on voltage, $V_G = V_{TO} = -0.1$ V and an "on" state with an I_D (= I_{ON}) of ≈8.5 μA at $V_G = V_{ON} = -0.8$ V, resulting in an on/off ratio of 10^3. Upon illumination with NIR light of intensity 0.8 mW cm^{-2}, as shown in Figure 2b, a third state, namely the "partially on" state, emerges in the transfer curve. I_D initially rises from $I_{OFF} = 0.01$ μA at $V_{TO} = -0.07$ V to a peak current or partially on current, $I_P = I_{PO} = 2.3$ μA at peak voltage, $V_P = -0.43$ V, then stabilizes until valley voltage, $V_V = -0.57$ V, followed by a second increase to reach the "on"

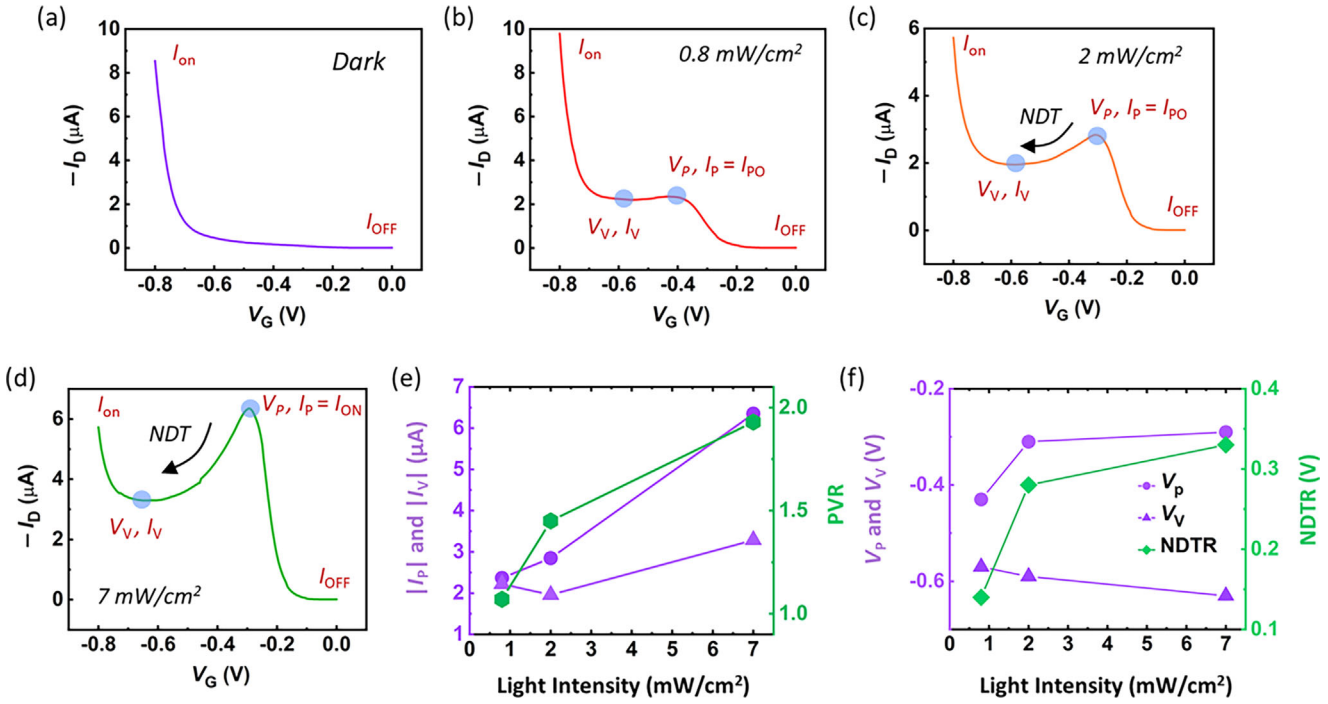

Figure 2. a–d) Transfer characteristics of the OECT under dark and increasing NIR light intensities. e) Variation of peak current, valley current, and peak-to-valley ratio as a function of light intensity. f) Variation of peak voltage, valley voltage, and NDT range with increasing NIR intensity.

state with a current, I_{ON} = 9.7 μA at V_{ON} = −0.8 V. Figure 2c shows that at a higher light intensity of 2 mW cm^{-2}, the non-monotonicity becomes more pronounced. I_D increases from I_{OFF} = 0.01 μA to $I_P = I_{PO}$ = 2.8 μA, then decreases to a valley current, I_V = 1.9 μA, before rising again to I_{ON} = 5.7 μA. Finally, Figure 2d shows that under even stronger illumination of 7 mW cm^{-2}, a pronounced NDT feature appears. I_D increases sharply from I_{OFF} = 0.01 μA to I_P = 6.4 μA, decreases to I_V = 3.3 μA and rises again to I_{ON} = 5.7 μA, giving rise to an "N"-shape transfer characteristics. Notably, this high-intensity condition gives rise to a three-level conduction configuration with two "on" states (I_P and I_{ON}) and one "off" state, establishing a multi-state switching mechanism. The emergence of NDT at high light intensity is also observed in the transconductance profile, which exhibits a peak negative transconductance (g_m) of −21 μS at V_G = −0.33 V under 7 mW cm^{-2} illumination (Figure S4, Supporting Information).

Figure 2e further quantifies the evolution of the photoresponse by tracking the key current states: I_P, I_V, and the peak-to-valley ratio (PVR = I_P / I_V) as a function of increasing NIR light intensity. As observed, I_P increases steadily from 2.4 to 6.3 μA when the NIR intensity is raised from 0.8 to 7 mW cm^{-2}, reflecting enhanced photo-induced hole density in the polymer channel. Alongside, I_V also increases from 2.2 to 3.3 μA with the increasing optical intensity. As a result, the PVR, a crucial figure of merit for evaluating the distinctiveness of the NDT response, increases from 1.1 to 1.9, indicating a sharper and more well-defined N-shaped transfer profile at higher light intensities. Additionally, Figure 2f captures the light-induced tuning of the V_P, V_V, and the NDT range (NDTR = | V_V − V_P |), providing insights into the voltage window over which the plateau or NDT occurs in the I_D. With increasing NIR intensity, V_P shifts positively from −0.43 to −0.29 V, while V_V shifts more negatively from −0.57 to −0.63 V, leading to a progressive expansion of NDTR from 0.14 to 0.34 V. This widened NDT range is also a crucial parameter; when leveraged in ternary logic circuits, it can enhance the noise margin of the intermediate logic state.[43] Hence, the light-intensity-dependent tuning of both PVR and NDTR offers a powerful degree of control over the OECT behavior, paving the way for light-programmable logic architectures.

Overall, by tuning the NIR light intensity, the OECT can be optically programmed into three distinct regimes: 1) a conventional binary "on/off" state under dark conditions, 2) a ternary "on/partially on/off" state at intermediate light levels, and 3) an "on/on/off" configuration featuring strong NDT at high illumination. This dynamic light-induced modulation of device characteristics holds significant promise for multifunctional and neuromorphic electronics. For instance, the ternary transfer profile with a distinguishable "partially on" state over a range of intermediate V_G is suitable for implementing ternary logic circuits, enabling compact and energy-efficient logic architectures beyond traditional binary design.[9–12] On the other hand, the on/on/off response under high-intensity NIR light, characterized by an NDT effect, can provide an intrinsic platform for emulating spiking neuronal behavior, something that typically requires complex circuitry involving multiple conventional transistors with monotonic transfer characteristics.[13,14] Moreover, the strong and tunable photoresponse highlights the potential of these devices for NIR sensing applications, where multi-state operation can be directly exploited for enhanced detection and signal encoding.

In addition to multifunctional programmability, the light-induced NDT response shows consistent behavior across multiple devices. As shown in Figure S5 (Supporting Information),

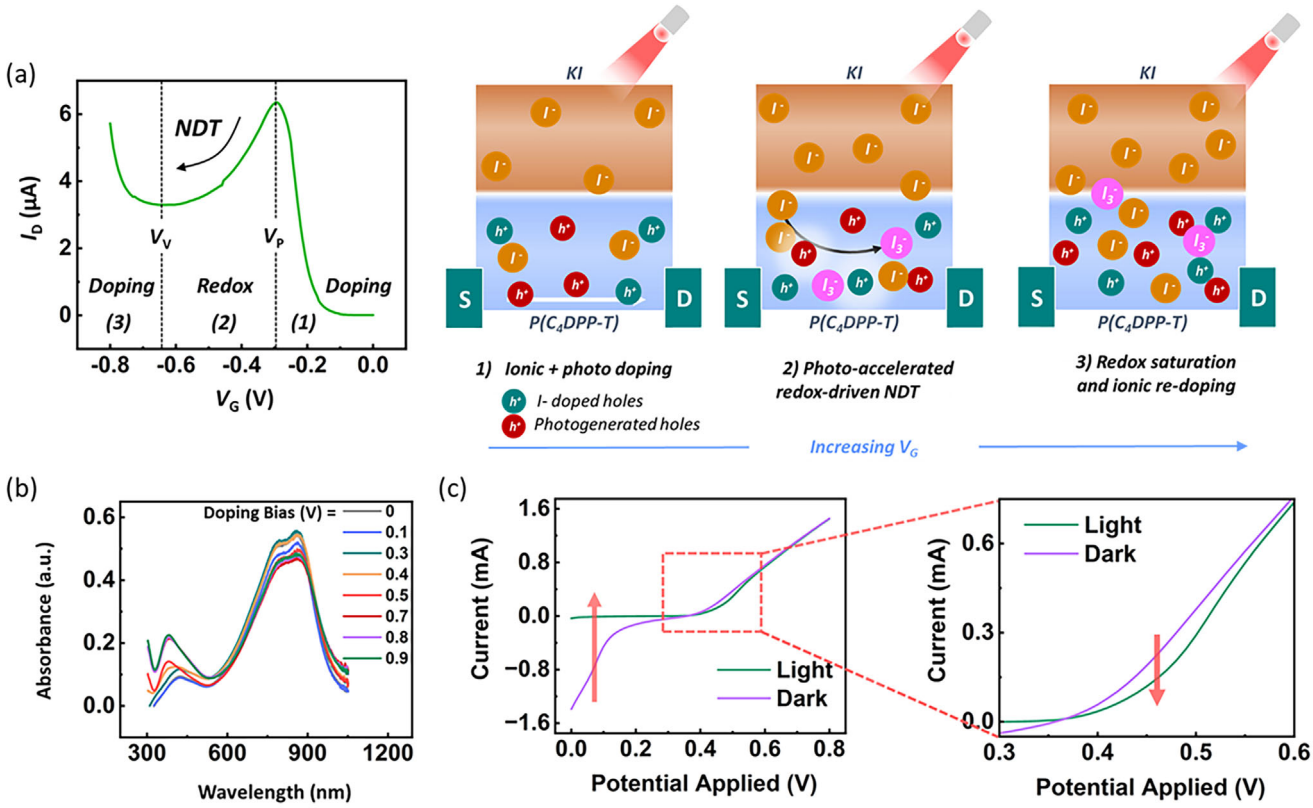

Figure 3. a) Transfer characteristics of p(C_4DPP-T)/KI OECT under NIR illumination, accompanied by schematics illustrating the dominant interfacial processes across three gate-voltage regimes: 1) ionic and photo-induced doping, 2) photo-accelerated redox-driven NDT, and 3) redox saturation followed by ionic re-doping. b) UV–vis absorption spectra of pristine and KI-doped p(C_4DPP-T) films. c) Cyclic voltammograms under dark and NIR conditions.

different devices exhibit a similar dark-to-NIR transformation from monotonic to N-shaped transfer profiles, confirming reliable device-to-device performance. The NDT characteristics also remain stable over repeated cycling (Figure S6, Supporting Information) and after 14 days of ambient storage (Figure S7, Supporting Information). Furthermore, even after 24 h immersion in KI electrolyte, the devices maintain comparable PVR values (Figure S8, Supporting Information), highlighting their operational durability.

Figure 3 lays out the light-driven mechanism responsible for the emergence of the N-shaped transfer response in the OECTs. The proposed mechanism follows a doping/redox/doping sequence, supported by electrochemical and spectroscopic analyses, including cyclic voltammetry and UV–vis absorption measurements. Iodine-based systems are known to undergo redox reactions leading to the formation of triiodide (I_3^-), while photogenerated holes further accelerate these conversions.[44–47] Our results indicate that NIR illumination in our system increases the hole population in p(C_4DPP-T), which promotes I_3^- formation and leads to the observed NDT response. Figure 3a shows the illuminated transfer curve divided into three V_G windows and the schematics that map the observed I_D evolution to the physical processes occurring within the electrolyte and polymer channel. **Range 1** ($0 < V_G < V_P$): As V_G increases, I^- ions are progressively driven toward the polymer, increasing the hole density in the channel and consequently, I_D rises. Under illumination, photo-induced holes further augment the carriers available for transport. Thus, the current rise in this range is governed primarily by field-driven hole accumulation, reinforced by photo-induced hole generation. **Range 2** ($V_P < V_G < V_V$): At intermediate V_G under light, the accumulated holes participate in redox reactions of iodide according to $2I^- + 2\,h$ (hole polaron) $\rightarrow I_2$, followed by $I_2 + I^- \leftrightarrow I_3^-$.[44–47] These reactions consume holes from the channel and transiently reduce the effective carrier density, producing the NDT region. To gain insight into this process, UV–vis absorption spectroscopy was performed during gradual electrochemical doping of the polymer with KI (Figure 3b). A new absorption band characteristic of triiodide (I_3^-) emerges near 372 nm and progressively intensifies between 0.4 and 0.7 V, confirming that the current suppression coincides with hole-consuming iodide oxidation.[48] The formation of triiodide was also confirmed by X-ray photoelectron spectroscopy (XPS), which shows no iodine signal at low bias (0.2 V), while distinct features emerge at ≈618.8 and ≈630.4 eV at 0.4 V and intensify further at 0.7 V, corresponding to the I $3d_{5/2}$ and I $3d_{3/2}$ components of I_3^- species (Figure S9, Supporting Information), indicating progressive conversion of iodide to triiodide under NIR-assisted electrochemical doping.[49] Cyclic voltammetry further supports this mechanism, exhibiting oxidation–reduction features characteristic of triiodide formation. A distinct color change from green to brown was observed during the CV scans (Figure S10, Supporting Information), consistent with the generation of triiodide species.

This finding is further corroborated by the starch–iodine test, which shows a transition to dark blue upon starch addition, confirming the formation of the [I_3^-·starch] complex (Figure S10, Supporting Information).[50] In contrast, under dark conditions, the hole population in the polymer remains lower and insufficient to sustain significant redox conversion, resulting in a predominantly monotonic p-type transfer response. Importantly, the NDT region appears only under NIR illumination. When exposed to visible light (400–700 nm), the device shows no NDT behavior (Figure S11, Supporting Information), as the polymer exhibits weak absorption in this range and cannot generate enough photo-induced holes to drive the iodide redox process. These results collectively confirm that photo-induced holes play a pivotal role in enabling the iodine-based redox reactions responsible for NDT, underscoring the necessity of NIR excitation. **Range 3** ($V_V < V_G < V_{ON}$): At higher V_G, the redox conversion of iodide reaches completion, as indicated by the saturation of the I_3^- absorption band (Figure 3b). Beyond this point, no further hole consumption occurs, and the redox contribution becomes negligible. The increasing V_G, at this stage, primarily drives additional I^- ions into the polymer, enhancing the doping process and restoring the hole density in the channel. As a result, I_D rises once more, completing the N-shaped transfer profile under illumination.

To gain further insight into the influence of NIR illumination, we compared the CV responses under light and dark conditions, as shown in Figure 3c. At low potentials ($0 < V < 0.35$ V), the current remains low in the dark because the applied bias is below the onset potential required to drive iodide oxidation; the small current in this regime primarily arises from capacitive charging of the polymer/electrolyte interface. Under illumination, the current increases strongly at low potentials due to photogenerated holes in the polymer. At intermediate potentials ($0.35 \text{ V} < V < 0.6$ V), the light-induced current drops below the dark current, indicating that the process transitions into a redox-dominated regime where holes are consumed through the oxidation of I^- to I_3^-. This transient current reduction is consistent with the NDT region observed in the transfer characteristics, arising from the competing dynamics of hole consumption and ionic doping. These observations confirm that NIR illumination accelerates iodide oxidation, enhances the I^- to I_3^- conversion, and thereby establishes the doping/redox/doping sequence responsible for the N-shaped transfer response. The complete CV cycle, including both forward and reverse scans, is presented in Figure S12 (Supporting Information), while the dependence of CV response on NIR intensity is shown in Figure S13 (Supporting Information). To further verify that iodide is essential for this photo-electrochemical redox process, we performed experiments using electrolytes containing other anions (Cl^-, Br^-, PF_6^-, $TFSI^-$, and SO_4^{2-}) under identical NIR illumination. None of these devices exhibited NDT behavior (Figure S14, Supporting Information), confirming that the absence of iodide prevents the interfacial redox reactions required for NDT. In contrast, devices operated with an ionic-liquid electrolyte containing iodide (EMIM-I) also showed NDT characteristics (Figure S15, Supporting Information), further validating that iodide-driven redox chemistry is necessary to trigger triiodide formation and the resulting antiambipolar response. Together, these results strongly support the proposed mechanism, establishing that NDT in these OECTs originates from I_3^- formation.

The evolution of V_P, V_V, NDTR, and PVR with NIR intensity, as observed in Figure 2e,f, can also be understood in light of the proposed doping/redox/doping mechanism. With increasing illumination intensity, V_P shifts toward lower V_G, reflecting the accelerated initiation of iodide oxidation under stronger photoexcitation. The higher density of photogenerated holes facilitates the earlier onset of the redox process, allowing the current peak to appear at a smaller V_G. In contrast, V_V shifts toward more negative V_G as the redox reaction becomes more complete and the system requires a larger potential to re-enter the doping-dominated regime. Consequently, the NDT region broadens with increasing NIR intensity, consistent with the prolonged dominance of redox-driven hole consumption. The corresponding increase in PVR arises because higher light intensity promotes a more extensive redox conversion, leading to a deeper transient current minimum and sharper contrast between the redox and re-doping phases. These results collectively demonstrate that NIR illumination governs the kinetics and balance of doping vs redox processes, thereby tuning both the position and strength of the N-shaped NDT response.

Building on this optical programmability, we next investigated whether the strength of the NDT response could be further tuned through device geometry, specifically by varying the gate/electrolyte interfacial area. While optical excitation generates additional mobile carriers and expands the NDT window, the ultimate current levels and sharpness of the NDT response are strongly governed by the capacitive coupling between the gate and the channel. Since this coupling is proportional to the gate/electrolyte interfacial area, controlling the gate size provides a direct way to amplify or suppress the NDT effect. In other words, NIR light acts as a dynamic, external stimulus to induce NDT, while the gate size governs the capacitive coupling that amplifies its magnitude.

Figure 4 illustrates the dependence of the NDT characteristics on the gate/electrolyte interfacial area under NIR illumination. To systematically investigate this effect, we varied the gate area from 1 mm^2 (small gate), 4 mm^2 (medium gate), to 9 mm^2 (large gate), as shown in Figure 4a–c. The corresponding transfer curves are presented in Figure 4d–f. For the small gate, I_D increases from $I_{OFF} = 7$ nA to $I_P = 250$ nA, then decreases to $I_V = 162$ nA before rising again to $I_{ON} = 306$ nA. When the gate area is increased to 4 mm^2, I_P rises significantly to 6.4 µA, followed by $I_V = 3.3$ µA, and a subsequent increase to $I_{ON} = 5.8$ µA. Further enlargement of the gate to 9 mm^2 results in an even higher $I_P = 15.5$ µA, $I_V = 5.6$ µA, and a recovery to $I_{ON} = 12.5$ µA. These results clearly indicate that increasing the gate/electrolyte interfacial area enhances both I_P and the overall current level of the OECTs. This behavior originates from the fact that a larger gate area provides a higher interfacial capacitance, which reduces the potential drop across the gate/electrolyte interface and directs more of the applied V_G to the semiconductor/electrolyte interface, thereby enabling stronger ionic doping and higher charge accumulation in the polymer channel.[51] The gate area dependence is further reflected in the extracted transconductance, g_m (Figure 4g). The maximum negative transonductance improves markedly with increasing gate area, from ≈1 µS for the small gate to 85 µS for the large gate. Similarly, the PVR shows a

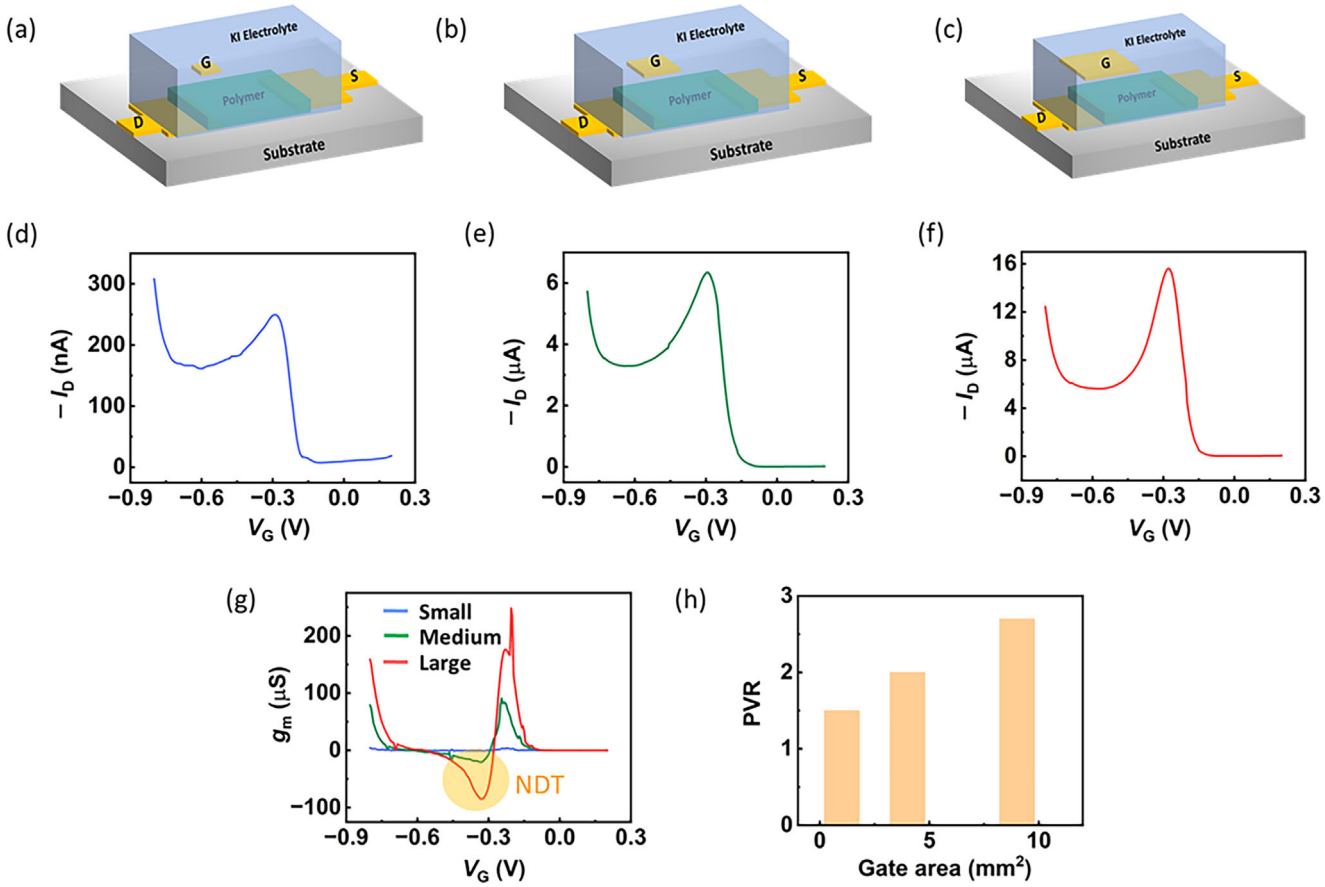

Figure 4. Device schematics with different gate electrode sizes: a) small, b) medium, and c) large. Transfer characteristics of the devices for d) small, e) medium, and f) large gate areas. g) Corresponding transconductance curves as a function of gate voltage h) Peak-to-valley ratio as a function of gate size.

monotonic improvement with gate size, increasing from 1.5 for the small gate to 2.7 for the large gate (Figure 4h). These results demonstrate that the NDT response in OECTs can be effectively tuned by capacitance engineering, where enlarging the gate/electrolyte interface amplifies the magnitude and sharpness of the NDT transition. Additional representative devices with the same gate-area configurations (Figure S16, Supporting Information) further validate this trend, confirming reproducible gate-geometry-dependent enhancement in NDT behavior.

Figure 5 summarizes the implementation of light-responsive logic circuits based on a current-driven OECT configuration. To examine the implications of optical reconfigurability, we employed an inverter-like topology in which the OECT is connected in series with a current source (Figure 5a). The input voltage (V_{IN}) is applied at the gate ($V_G = V_{IN}$), the output voltage (V_{OUT}) is measured at the drain, and a supply voltage (V_{DD}) is applied to the source. The drain current (I_{OUT}) is set by the bias current (I_B) provided by a current source, making the OECT the primary active element.[52]

Under dark conditions (Figure 5b), this configuration delivers conventional binary logic behavior. Specifically, **Logic state "1"**: At strongly negative V_{IN}, the OECT is fully on, exhibiting low channel resistance (R_o), and a high drain current ($I_D > I_B$). Consequently, V_{OUT} approaches V_{DD}, since $V_{OUT} = V_{DD} - I_B \times R_o$. **Logic state "0"**: As V_{IN} becomes less negative, the device turns off, leading to a significant increase in R_o with $I_D < I_B$, driving V_{OUT} toward $-V_{DD}$. Illumination significantly alters this landscape on the fly. As shown in Figure 5c, under NIR exposure, the OECT develops NDT characteristics, enabling ternary logic with three distinct states. **Logic state "1"**: At large negative V_G, the OECT is in the on state with low R_o, resulting in $V_{OUT} \approx V_{DD}$. **Logic state "½"**: Within the NDT region, I_D balances the bias current I_B, causing V_{OUT} to stabilize between V_{DD} and $-V_{DD}$. **Logic state "0"**: At weak V_G, the channel resistance becomes large, and V_{OUT} approaches $-V_{DD}$.

A schematic in Figure 5d illustrates this light-controlled switching between binary and ternary logic regimes. This dynamic reconfigurability, achieved through optical stimulus, paves the way for multifunctional circuit elements capable of adapting their logic behavior in situ. Such systems can be useful in smart sensor interfaces, light-sensitive decision-making systems, multivalued logic circuits, and neuromorphic devices. The seamless and reversible nature of this reconfiguration highlights a promising direction for next-generation organic and hybrid electronics, where computation and sensing are tightly integrated within a single adaptive platform.

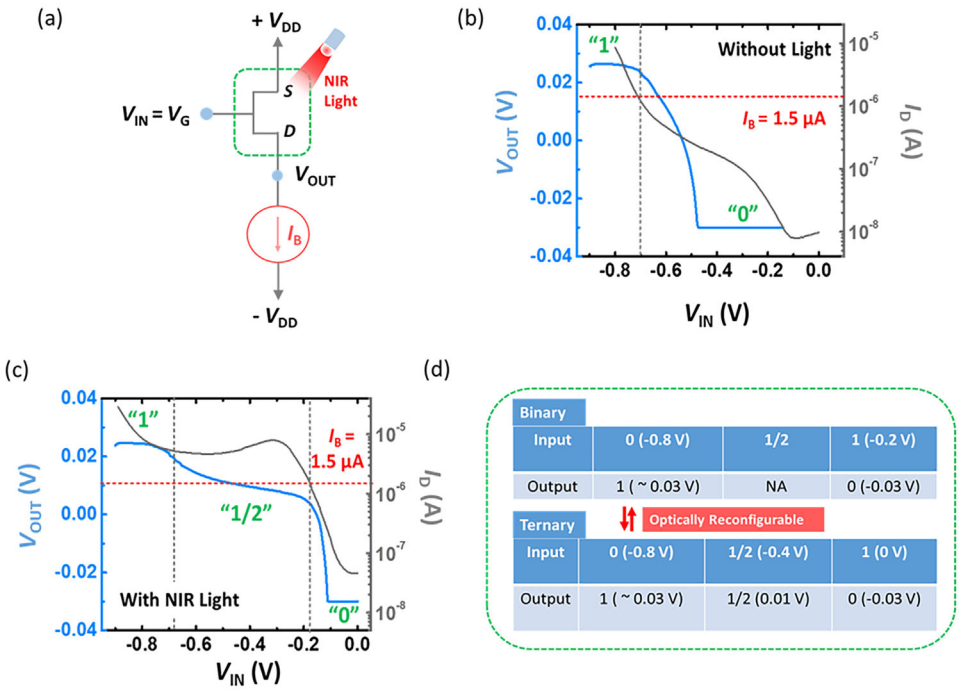

Figure 5. a) Circuit schematic of the current-driven OECT. b) Voltage transfer characteristics (VTC, blue line) of the circuit in the dark, shown alongside the OECT transfer curve (black line) without a current source. c) VTC of the circuit under 7 mW cm^{-2} NIR illumination, with the corresponding OECT characteristics. d) Schematic illustration of optically induced logic reconfigurability, highlighting transitions between binary and ternary logic states.

3. Conclusion

In conclusion, we have demonstrated a simple yet efficient strategy to induce and control NDT characteristics in OECTs using NIR illumination. By combining a NIR-absorbing polymer, p(C_4DPP-T), with a KI-based electrolyte, the devices transition from conventional binary switching to ternary operation, with well-defined multistate responses emerging under controlled optical excitation. The NDT behavior originates from light-induced hole generation in the polymer coupled with iodide redox processes leading to triiodide formation. We further showed that the sharpness and strength of the NDT effect can be enhanced by enlarging the gate/electrolyte interface, underscoring geometry as an effective design lever to complement optical control. The resulting "N"-shaped transfer characteristics were successfully exploited in optically reconfigurable inverter circuits, enabling seamless switching between binary and ternary logic modes. This light-driven adaptability establishes OECTs as a versatile platform for future optoelectronic technologies that unify logic, neuromorphic computing, and multifunctional sensing in a single device.

4. Experimental Section

Organic electrochemical transistors were fabricated on standard glass microscope slides (75 mm × 25 mm) that were cleaned by ultrasonication in a Micro-90 detergent solution, rinsed, and sonicated in a 1:1 acetone–isopropanol mixture, followed by N_2 drying.

Gold source, drain, and gate electrodes were patterned by standard lift-off photolithography. A positive photoresist (Microposit S1813) was spin-coated, soft-baked at 110 °C for 60 s, and exposed through a photomask using a mask aligner. The resist was developed in MF-26A developer and rinsed with deionized water. A thin adhesion layer of Cr (5 nm) followed by Au (80 nm) was then deposited by sputtering. Lift-off was performed in acetone (6 h sonication), resulting in well-defined coplanar source, drain, and gate electrodes on the same substrate.

Two layers of parylene-C were subsequently deposited. A 1% (v/v) Micro-90 soap solution was spin-coated between the layers to enable the selective removal of the upper parylene layer, while the bottom layer electrically insulated the electrodes.

The transistor channel opening was defined via a second photolithography step, aligned to the first electrode mask using optical alignment marks to ensure accurate registration with the metal contacts. After exposure and development, the parylene-C in the channel region was etched using reactive-ion etching (O_2/CHF_3 plasma, 160 W, 16 min; 50 sccm O_2/5 sccm CHF_3), exposing the channel area between source and drain.

A p(C_4DPP-T) semiconductor solution (5 mg mL^{-1} in chloroform) was spin-coated at 1000 rpm to yield a ≈90 nm film. A soft-bake was performed at 60 °C for 1 min, after which the sacrificial parylene-C layer was peeled off using adhesive tape, leaving the polymer only in the defined channel window with precise alignment to the electrodes. A final annealing step at 60 °C for 15 min completed the device fabrication. Channel length and width were 100 and 25 µm, respectively. Electrical measurements, including current–voltage characterization, were performed using a Keithley 2400 SourceMeter.

Cyclic voltammetry (CV) measurements were carried out under ambient conditions using a standard three-electrode configuration. An aqueous 10 mM KI solution was used as the electrolyte, with a scan rate of 15 mV s^{-1}. An Ag/AgCl aqueous reference electrode and a platinum counter electrode were employed, while the working electrode consisted of polymers spin-coated on ITO substrates. All potentials were measured relative to the Ag/AgCl reference electrode. For absorption and XPS measurements, the films were doped by applying fixed potentials during CV at different bias conditions, and spectra were recorded at each bias point.

Supporting Information

Supporting Information is available from the Wiley Online Library or from the author.

Acknowledgements

This work was supported by the Alexander von Humboldt Foundation, which provided funding for research materials and experimental infrastructure. The authors gratefully acknowledge Helma Burg and Rüdiger Berger of the Atomic Force Microscopy Core Facility for their assistance with AFM measurements, and Leon Prädel for performing the XPS measurements. The authors also thank Michelle Beuchel, Christian Bauer, and Sirma Koynova for their technical contributions.

Conflict of Interest

The authors declare no conflict of interest.

Data Availability Statement

The data that support the findings of this study are available in the supplementary material of this article.

Keywords

antiambipolar behavior, near-infrared (NIR) light programmability, negative differential transconductance, optically reconfigurable logic, organic electrochemical transistor

Received: September 22, 2025
Revised: November 11, 2025
Published online:

[1] S. Wang, X. Chen, C. Zhao, Y. Kong, B. Lin, Y. Wu, Z. Bi, Z. Xuan, T. Li, Y. Li, W. Zhang, *Nat. Electron.* **2023**, *6*, 281.
[2] L. Salvigni, P. D. Nayak, A. Koklu, D. Arcangeli, J. Uribe, A. Hama, R. Silva, T. C. Hidalgo Castillo, S. Griggs, A. Marks, I. McCulloch, *Nat. Commun.* **2024**, *15*, 6499.
[3] A. Saleh, A. Koklu, I. Uguz, A. M. Pappa, S. Inal, *Nat. Rev. Bioeng.* **2024**, *2*, 559.
[4] P. C. Harikesh, D. Tu, S. Fabiano, *Nat. Electron.* **2024**, *7*, 525.
[5] C. Lubrano, U. Bruno, C. Ausilio, F. Santoro, *Adv. Mater.* **2022**, *34*, 2110194.
[6] A. Makhinia, K. Hübscher, V. Beni, P. A. Ersman, *Adv. Mater. Technol.* **2022**, *7*, 2200153.
[7] A. Nawaz, Q. Liu, W. L. Leong, K. E. Fairfull-Smith, P. Sonar, *Adv. Mater.* **2021**, *33*, 2101874.
[8] M. Cucchi, D. Parker, E. Stavrinidou, P. Gkoupidenis, H. Kleemann, *Adv. Mater.* **2023**, *35*, 2209516.
[9] K. Kobashi, R. Hayakawa, T. Chikyow, Y. Wakayama, *Nano Lett.* **2018**, *18*, 4355.
[10] H. Yoo, S. On, S. B. Lee, K. Cho, J. J. Kim, *Adv. Mater.* **2019**, *31*, 1808265.
[11] D. Panigrahi, R. Hayakawa, J. Aimi, Y. Wakayama, *Adv. Mater. Technol.* **2023**, *8*, 2301049.
[12] Z. Zhang, S. Huo, Q. Tian, F. Meng, Z. Yang, Y. Ma, Y. Wang, Y. Xie, X. Hu, W. Gao, E. Wu, *Adv. Funct. Mater.* **2025**, *35*, 2424728.
[13] C. Wan, M. Pei, K. Shi, H. Cui, H. Long, L. Qiao, Q. Xing, Q. Wan, *Adv. Mater.* **2024**, *36*, 2311288.
[14] T. Sarkar, K. Lieberth, A. Pavlou, T. Frank, V. Mailaender, I. McCulloch, P. W. M. Blom, F. Torricelli, P. Gkoupidenis, *Nat. Electron.* **2022**, *5*, 774.
[15] Y. Meng, W. Wang, W. Wang, B. Li, Y. Zhang, J. Ho, *Adv. Mater.* **2024**, *36*, 2306290.
[16] Y. Wakayama, C. H. Kim, D. Panigrahi, R. Hayakawa, *Mater. Adv.* **2022**, *3*, 5260.
[17] H. Son, J. Lee, T. H. Kim, S. Choi, H. Choi, Y. H. Kim, S. Lee, *Appl. Surf. Sci.* **2022**, *581*, 152396.
[18] S. Sen, F. Capasso, F. Beltram, A. Y. Cho, *IEEE Trans. Electron Devices* **1987**, *34*, 1768.
[19] J. C. Shin, J. H. Lee, M. Jin, H. Lee, J. Kim, J. Lee, C. Lee, W. You, H. Yang, Y. S. Kim, *ACS Nano* **2024**, *18*, 1543.
[20] Y. Liu, J. Guo, Q. He, H. Wu, H. C. Cheng, M. Ding, I. Shakir, V. Gambin, Y. Huang, X. Duan, *Nano Lett.* **2017**, *17*, 5495.
[21] Z. Deng, Y. Yu, Y. Zhou, J. Zhou, M. Xie, B. Tao, Y. Lai, J. Wen, Z. Fan, X. Liu, D. Zhao, *Adv. Mater.* **2024**, *36*, 2405115.
[22] X. Wu, Q. He, Z. Zhou, T. L. D. Tam, C. Tang, M. Lin, M. Moser, S. Griggs, A. Marks, S. Chen, J. Xu, *Adv. Mater.* **2024**, *36*, 2308823.
[23] P. C. Harikesh, C. Y. Yang, H. Y. Wu, S. Zhang, M. J. Donahue, A. S. Caravaca, J. D. Huang, P. S. Olofsson, M. Berggren, D. Tu, S. Fabiano, *Nat. Mater.* **2023**, *22*, 242.
[24] B. D. Paulsen, C. D. Frisbie, *J. Phys. Chem. C* **2012**, *116*, 3132.
[25] Z. Laswick, X. Wu, A. Surendran, Z. Zhou, X. Ji, G. M. Matrone, W. L. Leong, J. Rivnay, *Nat. Commun.* **2024**, *15*, 6309.
[26] D. Panigrahi, R. Hayakawa, J. Zhong, J. Aimi, Y. Wakayama, *Adv. Funct. Mater.* **2023**, *33*, 2213899.
[27] D. Panigrahi, R. Hayakawa, X. Zhong, J. Aimi, Y. Wakayama, *Nano Lett.* **2023**, *23*, 319.
[28] C. Lee, C. Lee, S. Lee, J. Choi, H. Yoo, S. G. Im, *Nat. Commun.* **2023**, *14*, 3757.
[29] D. U. Lim, S. B. Jo, J. H. Cho, *Adv. Mater.* **2023**, *35*, 2208757.
[30] G. Gao, J. H. Chen, M. J. Jing, J. Hu, Q. Xu, C. S. Wang, H. Zhou, P. Lin, G. Chen, W. W. Zhao, *Adv. Funct. Mater.* **2023**, *33*, 2300580.
[31] B. Y. Zhou, Y. T. Huang, C. Yuan, H. Lou, X. S. Liu, W. W. Zhao, H. Y. Chen, J. J. Xu, *Adv. Funct. Mater.* **2024**, *34*, 2405913.
[32] P. Qu, C. J. Li, J. Hu, G. Gao, P. Lin, W. W. Zhao, *Anal. Chem.* **2023**, *95*, 9983.
[33] S. Xiao, T. Zheng, W. Chen, J. Zhang, M. Yang, Y. Sun, Z. Zheng, D. Hao, N. Huo, Z. Chen, W. Gao, *Adv. Funct. Mater.* **2024**, *34*, 2403509.
[34] Z. Wu, Y. Wang, Y. Dou, L. Zhou, J. Zhu, *Nano Res. Energy* **2023**, *2*, 9120080.
[35] X. Gao, Q. Chen, Q. Qin, L. Li, M. Liu, D. Hao, J. Li, J. Li, Z. Wang, Z. Chen, *Nano Res.* **2024**, *17*, 1886.
[36] Y. D. Kenry, B. Liu, *Adv. Mater.* **2018**, *30*, 1802394.
[37] R. Vitorino, A. S. Barros, S. Guedes, D. C. Caixeta, R. Sabino-Silva, *Photodiagn. Photodyn. Ther.* **2023**, *42*, 103633.
[38] Y. A. Kwon, S. B. Park, J. Kim, Y. Yoo, S. W. Lee, J. H. Cho, *Nat. Commun.* **2025**, *16*, 6740.
[39] J. C. Shin, C. Lee, J. Lee, J. Kim, J. A. Jeon, H. Yang, M. Jin, Y. S. Kim, *Small* **2025**, *21*, 2501543.
[40] B. Kolodziejczyk, C. H. Ng, X. Strakosas, G. G. Malliaras, B. Winther-Jensen, *Mater. Horiz.* **2018**, *5*, 93.
[41] V. Druet, D. Ohayon, C. E. Petoukhoff, Y. Zhong, N. Alshehri, A. Koklu, P. D. Nayak, L. Salvigni, L. Almulla, J. Surgailis, S. Griggs, *Nat. Commun.* **2023**, *14*, 5481.
[42] Y. Yan, X. Wu, Q. Chen, Y. Liu, H. Chen, T. Guo, *ACS Appl. Mater. Interfaces* **2019**, *11*, 20214.
[43] D. Panigrahi, R. Hayakawa, Y. Wakayama, *J. Mater. Chem. C* **2022**, *10*, 5559.
[44] M. Skunik-Nuckowska, J. Lubera, P. Rączka, A. A. Mroziewicz, S. Dyjak, P. J. Kulesza, *ChemElectroChem* **2022**, *9*, 202101222.
[45] G. F. Samu, Á. Balog, F. De Angelis, D. Meggiolaro, P. V. Kamat, C. Janáky, *J. Am. Chem. Soc.* **2019**, *141*, 10812.

[46] A. Turolla, A. Piazzoli, J. F. Budarz, M. R. Wiesner, M. Antonelli, *Chem. Eng. J.* **2015**, *271*, 260.
[47] C. Karunakaran, S. Senthilvelan, S. Karuthapandian, K. Balaraman, *Catal. Commun.* **2004**, *5*, 283.
[48] S. Moulay, *J. Polym. Eng.* **2013**, *33*, 389.
[49] J. Yu, L. Song, B. Han, J. Hu, Z. Li, J. Mi, *Polymers* **2024**, *16*, 2846.
[50] S. Pesek, M. Lehene, A. M. Brânzanic, R. Silaghi-Dumitrescu, *Molecules* **2022**, *27*, 8974.
[51] K. G. Cho, K. H. Lee, C. D. Frisbie, *ACS Appl. Mater. Interfaces* **2024**, *16*, 19309.
[52] M. Ghittorelli, L. Lingstedt, P. Romele, N. I. Crăciun, Z. M. Kovács-Vajna, P. W. M. Blom, F. Torricelli, *Nat. Commun.* **2018**, *9*, 1441.